The redshift evolution of ΛCDM halo parameters: concentration, spin and shape

J.C. Muñoz-Cuartas[1]*, A.V. Macciò[2], S.Gottlöber[1], A.A. Dutton[3]†

[1] *Astrophysikalisches Institut Potsdam, An der Sternwarte 16, 14482 Potsdam, Germany.*
[2] *Max-Planck-Institut Für Astronomie, Königstuhl 17, 69117 Heidelberg, Germany.*
[3] *Department of Physics and Astronomy, University of Victoria, Victoria, B.C., V8P 5C2, Canada.*

ABSTRACT

We present a detailed study of the redshift evolution of dark matter halo structural parameters in a ΛCDM cosmology. We study the mass and redshift dependence of the concentration, shape and spin parameter in N-body simulations spanning masses from $10^{10}\ h^{-1}\,\mathrm{M_\odot}$ to $10^{15}\ h^{-1}\,\mathrm{M_\odot}$ and redshifts from 0 to 2. We present a series of fitting formulae that accurately describe the time evolution of the concentration–mass ($\mathrm{c_{vir}} - \mathrm{M_{vir}}$) relation since $z = 2$. Using arguments based on the spherical collapse model we study the behaviour of the scale length of the density profile during the assembly history of haloes, obtaining physical insights on the origin of the observed time evolution of the $\mathrm{c_{vir}} - \mathrm{M_{vir}}$ relation. We also investigate the evolution with redshift of dark matter halo shape and its dependence on mass. Within the studied redshift range the relation between halo shape and mass can be well fitted by a redshift dependent power law. Finally we show that although for $z = 0$ the spin parameter is practically mass independent, at increasing redshift it shows a increasing correlation with mass.

Key words: galaxies: haloes – cosmology:theory, dark matter, gravitation – methods: numerical, N-body simulation

1 INTRODUCTION

Observational evidence (e.g. Spergel et al. 2007; Komatsu et al. 2009) favours the hierarchical growth of structures in a universe dominated by cold dark matter (CDM) and dark energy (Λ), the so called ΛCDM universe. Within this paradigm dark matter collapses first into small haloes which accrete matter and merge to form progressively larger haloes over time. Galaxies are thought to form out of gas which cools and collapses to the centres of these dark matter haloes (e.g. White & Rees 1978). In this picture the properties of galaxies are expected to be strongly related to the properties of the dark matter haloes in which they are embedded (e.g. Mo, Mao & White 1998, Dutton et al. 2007).

It has been shown by several studies that the structural properties of dark matter (DM) haloes are dependent on halo mass: for example higher mass haloes are less concentrated (Navarro, Frank & White 1997, hereafter NFW; Eke et al. 2001; Bullock et al. 2001a; Kuhlen et al. 2005; Macciò et al. 2007; Neto et al. 2007; Gao et al. 2008; Duffy et al. 2008; Macciò, Dutton, & van den Bosch 2008 (hereafter M08); Klypin et al. 2010), and are more prolate (Jing & Suto

2002; Allgood et al. 2006; Gottlöber & Yepes 2007; Bett et al. 2007; Macciò et al. 2007; M08) on average. The situation is less clear for the spin parameter, at $z = 0$ there seems to be no mass dependence (Macciò et al. 2007; M08) or at least a very weak one (Bett et al. 2007), while for increasing values of the redshift a possible mild correlation between spin and mass seems to arise (Knebe & Power 2008).

In M08 the properties of DM haloes were studied in ΛCDM universes whose parameters were fixed by the one, three and five-year release of the WMAP mission (WMAP5; Komatsu et al. 2009). In that study the attention has been focused on the structural parameters of virialized haloes and their correlations at the present epoch, $z = 0$. In this work we extend this previous analysis to higher redshifts and study how the scaling relations of DM haloes change with time.

As in M08 we use a large suite of N-body simulations in a WMAP5 cosmology with different box sizes to cover the entire halo mass range relevant for galaxy formation: from $10^{10}h^{-1}\,\mathrm{M_\odot}$ (haloes that host dwarf galaxies) to $10^{15}h^{-1}\,\mathrm{M_\odot}$ (massive clusters). We use these simulations to investigate the evolution of concentrations, spin parameter and shapes of dark matter haloes through cosmic time.

Similar studies have been already conducted in the past,

* Email : jcmunoz@aip.de
† CITA National Fellow

mainly using lower numerical resolution and/or a smaller mass range (but with few recent exceptions).

Navarro, Frank & White (1997) proposed that the characteristic density of dark matter haloes was directly proportional to the density of the universe at time of formation, making possible to connect today properties of the dark matter density profile to the halo formation history and to the evolution of the expanding universe. This idea was then expanded by Wechsler et al. (2002), who found a clear connection between the mass growth of dark matter haloes and the definition of the formation time; connecting directly the growth history of dark matter haloes to the evolution of their concentration parameter.

In a series of papers, Zhao et al. (2003a, 2003b, 2009) have re-addressed the problem of the evolution of dark matter halo density profile and the mass accretion history. Zhao's main result was the finding of a correlation between r_s and the characteristic mass of dark matter haloes, M_s, defined as the mass inside r_s. Thanks to this correlation they were able to model the time evolution of the concentration parameter in a cosmology-free fashion.

A comparison of the different approaches to predict dark matter halo concentrations was performed by Neto et al. (2007). They made a detailed comparison of the Wechsler et al. (2002) and Zhao et al. (2003) models for the time evolution of dark matter halo masses and their resulting predictions for halo concentration. Neto et al. (2007) found that although these models could match the average concentration reasonably well, they performed very poorly in many cases, because their models for halo mass evolution were not able to satisfactorily reproduce "real" mass growth histories from N-body simulations.

However, the evolution of dark matter halo properties does not reduce to the concentration parameter only; halo shape and spin parameter are also important quantities that could influence the properties of the hosted galaxy. Allgood et al. (2006) studied the mass, radius, redshift and cosmology dependence (via variations of σ_8) of the shape of dark matter haloes; while the environment dependence of the shape has been addressed in Hahn et al. (2007a,b). The distribution of the spin parameter of dark matter haloes has been studied in several works (e.g. Bullock et al. 2001b; Macciò et al. 2007; Bett et al. 2007; M08; Knebe & Power 2008; Davis & Natarajan 2009; Antonuccio-Delogu et al. 2010) as well as the correlation between halo angular momentum and large scale structure (e.g. Bailin & Steinmetz 2005, Bett et al. 2010). One of the conclusions was that the correlation between spin and mass (almost absent at $z = 0$) seems to increase with increasing redshift. Such a behavior could have important influences in the modeling of properties of galaxies at high redshift.

Although it has been shown that the inclusion of baryonic physics may affect the properties of the dark matter distribution (e.g. Gnedin et al. 2004, Kazantzidis et al. 2004, Libeskind et al. 2010, Knebe et al. 2010, Bett et al. 2010), it also known that the strength of this effect strongly depends on the implemented baryonic physics (Duffy et al. 2010). The aim of this work is to extend the findings of M08 to higher redshift and to provide a comprehensive study of the evolution and correlation of the properties of DM haloes from $z = 2$ to the present day. Such a study is a basic ingre-

Name	Box Size	N	m_i	ϵ	$N_{min} > 500$ z=0,2
B20	14.4	250^3	1.37e7	0.43	974, 1006
B30	21.6	300^3	2.68e7	0.64	1515, 1399
B40	28.8	250^3	1.10e8	0.85	1119, 993
B90	64.8	600^3	9.04e7	0.85	13587, 12177
B180	129.6	300^3	5.78e9	3.83	2300, 510
B300	216.0	400^3	1.13e10	4.74	5840, 707
B300$_2$	216.0	400^3	1.13e10	4.74	5720, 766

Table 1. Table of simulations used in this work. Note that the name of the simulation is related to the box size in units of Mpc. N represents the number of total particles in the box. ϵ represents the force softening length in units of kpc h^{-1} and the last column gives the number of haloes with more than 500 particles at $z = 0$ and $z = 2$. Masses of particles are in units of $h^{-1} \, M_\odot$ and box sizes in units of Mpc h^{-1}, with $h = 0.72$.

dient to understand the complex problem of galaxy formation and evolution.

Our paper is organized as follows. In Section 2 we describe the set of simulations we used, present definitions and describe the numerical procedures. In Section 3 we present our results for the mass and redshift dependence of the concentration parameter, present a novel and physically motivated approach to understand the time evolution of the concentration parameter following arguments based on the spherical collapse model. Next we discuss our results for the mass and redshift dependence of the shape (Section 4) and spin parameter (Section 5). Finally in Section 6 we summarize our findings and discuss on our results and their influence on the modeling of galaxy properties.

2   NUMERICAL SIMULATIONS

All simulations have been performed with PKDGRAV, a tree code written by Joachim Stadel and Thomas Quinn (Stadel 2001). The code uses spline kernel softening, for which the forces become completely Newtonian at 2 softening lengths. Individual time steps for each particle are chosen proportional to the square root of the softening length, ϵ, over the acceleration, a: $\Delta t_i = \eta \sqrt{\epsilon/a_i}$. Throughout, we set $\eta = 0.2$, and we keep the value of the softening length constant in comoving coordinates during each run. The physical values of ϵ at $z = 0$ are listed in Table 1. Forces are computed using terms up to hexadecapole order and a node-opening angle θ which we change from 0.55 initially to 0.7 at $z = 2$. This allows a higher force accuracy when the mass distribution is nearly smooth and the relative force errors can be large. The initial conditions are generated with the GRAFIC2 package (Bertschinger 2001). The starting redshifts z_i are set to the time when the standard deviation of the smallest density fluctuations resolved within the simulation box reaches 0.2 (the smallest scale resolved within the initial conditions is defined as twice the intra-particle distance).

Table 1 lists all of the simulations used in this work. We have run simulations for several different box sizes, which allows us to probe halo masses covering the entire range 10^{10} $h^{-1} \, M_\odot < M < 10^{15} h^{-1} \, M_\odot$. In addition, in some cases we have run multiple simulations for the same cosmology and

box size, in order to test for the impact of cosmic variance (and to increase the final number of dark matter haloes).

In all of the simulations, dark matter haloes are identified using a spherical overdensity (SO) algorithm. We use a time varying virial density contrast determined using the fitting formula presented in Bryan and Norman (1998). We include in the halo catalogue all the haloes with more than 500 particles inside the virial radius ($N_{\rm vir} > 500$).

We have set the cosmological parameters according to the fifth-year results of the Wilkinson Microwave Anisotropy Probe mission (WMAP5, Komatsu et al. 2009), namely, $\Omega_m = 0.258$, $\Omega_L = 0.742$, $n = 0.963$, $h = 0.72$, and $\sigma_8 = 0.796$, where Ω_m and Ω_L are the values of the density parameters at z=0.

2.1 Halo parameters

For each SO halo in our sample we determine a set of parameters, including the virial mass and radius, the concentration parameter, the angular momentum, the spin parameter and axis ratios (shape). Below we briefly describe how these parameters are defined and determined. A more detailed discussion can be found in Macciò et al. (2007, 2008).

2.1.1 Concentration parameter

To compute the concentration of a halo we first determine its density profile. The halo centre is defined as the location of the most bound halo particle (we define the most bound particle as the particle with the lowest potential energy, no care about binding energy is taken here), and we compute the density (ρ_i) in 50 spherical shells, spaced equally in logarithmic radius. Errors on the density are computed from the Poisson noise due to the finite number of particles in each mass shell. The resulting density profile is fitted with a NFW profile:

$$\frac{\rho(r)}{\rho_c} = \frac{\delta_{\rm c}}{(r/r_{\rm s})(1 + r/r_{\rm s})^2}, \tag{1}$$

During the fitting procedure we treat both $r_{\rm s}$ and δ_c as free parameters. Their values, and associated uncertainties, are obtained via a χ^2 minimization procedure using the Levenberg & Marquardt method. We define the r.m.s. of the fit as:

$$\rho_{\rm rms} = \frac{1}{N} \sum_i^N \left(\ln \rho_i - \ln \rho_{\rm m} \right)^2 \tag{2}$$

where $\rho_{\rm m}$ is the fitted NFW density distribution.[1] Finally, we define the concentration of the halo, $c_{\rm vir} \equiv R_{\rm vir}/r_{\rm s}$, using the virial radius obtained from the SO algorithm, and we define the error on $\log c$ as $(\sigma_{r_{\rm s}}/r_{\rm s})/\ln(10)$, where $\sigma_{r_{\rm s}}$ is the fitting uncertainty on $r_{\rm s}$.

---

[1] A more conservative notation for the r.m.s of the fit would be σ_ρ^2. Nevertheless we keep the use of $\rho_{\rm rms}$ to be consistent with the notation used in Macciò et al. (2007, 2008)

2.1.2 Spin parameter

The spin parameter is a dimensionless measure of the amount of rotation of a dark matter halo. We use the definition introduced by Bullock et al. (2001b):

$$\lambda' = \frac{J_{\rm vir}}{\sqrt{2}M_{\rm vir}V_{\rm vir}R_{\rm vir}} \tag{3}$$

where $M_{\rm vir}$ is the mass interior to $R_{\rm vir}$, $J_{\rm vir}$ is the total angular momentum of that mass distribution and $V_{\rm vir}$ is its circular velocity at the virial radius. See Macciò et al. (2007) for a detailed discussion and for a comparison of the different definitions of the spin parameter.

2.1.3 Shape parameter

Determining the shape of a three-dimensional distribution of particles is a non-trivial task (e.g., Jing & Suto 2002). Following Allgood et al. (2006), we determine the shapes of our haloes starting from the inertia tensor. As a first step, we compute the halo's 3×3 inertia tensor using all the particles within the virial radius. Next, we diagonalize the inertia tensor and rotate the particle distribution according to the eigenvectors. In this new frame (in which the moment of inertia tensor is diagonal) the ratios a_3/a_1 and a_3/a_2 (where $a_1 \geqslant a_2 \geqslant a_3$) are given by:

$$\frac{a_3}{a_1} = \sqrt{\frac{\sum m_i z_i^2}{\sum m_i x_i^2}} \qquad \frac{a_3}{a_2} = \sqrt{\frac{\sum m_i z_i^2}{\sum m_i y_i^2}}. \tag{4}$$

Next we again compute the inertia tensor, but this time only using the particles inside the ellipsoid defined by a_1, a_2, and a_3. When deforming the ellipsoidal volume of the halo, we keep the longest axis (a_1) equal to the original radius of the spherical volume ($R_{\rm vir}$). We iterate this procedure until we converge to a stable set of axis ratios. Although this iterative procedure can indeed change the mass contained inside of the ellipsoid, we checked that variations are nevertheless below 20%. We will therefore not consider those changes in mass when showing mass-shape relations, and we will work always with virial masses.

2.2 Relaxed - Unrelaxed haloes

Our halo finder (and halo finders in general) does not distinguish between relaxed and unrelaxed haloes. There are many reasons why we might want to remove unrelaxed haloes. First and foremost, unrelaxed haloes often have poorly defined centers, which makes the determination of a radial density profile, and hence of the concentration parameter, an ill-defined problem. Moreover unrelaxed haloes often have shapes that are not adequately described by an ellipsoid, making our shape parameters ill-defined as well.

Following Macciò et al. (2007), we decide to use a combination of two different parameters $\rho_{\rm rms}$ and $x_{\rm off}$ to determine the dynamical status of a given dark matter halo. The first quantity $\rho_{\rm rms}$ is defined as the r.m.s. of the NFW fit to the density profile (performed to compute c_{vir}). While it is true that $\rho_{\rm rms}$ is typically high for unrelaxed haloes, haloes with relatively few particles also have a high $\rho_{\rm rms}$ (due to Poisson noise) even when they are relaxed; furthermore, since the spherical averaging used to compute the density profiles

has a smoothing effect, not all unrelaxed haloes have a high $\rho_{\rm rms}$. In order to circumvent these problems, we combine the value of $\rho_{\rm rms}$ with the $x_{\rm off}$ parameter, defined as the distance between the most bound particle (used as the center for the density profile) and the center of mass of the halo, in units of the virial radius. This offset is a measure for the extent to which the halo is relaxed: relaxed haloes in equilibrium will have a smooth, radially symmetric density distribution, and thus an offset that is virtually equal to zero. Unrelaxed haloes, such as those that have only recently experienced a major merger, are likely to reveal a strongly asymmetric mass distribution, and thus a relatively large $x_{\rm off}$. Although some unrelaxed haloes may have a small $x_{\rm off}$, the advantage of this parameter over, for example, the actual virial ratio, $2T/V$, as a function of radius (e.g. Macciò, Murante & Bonometto 2003), is that the former is trivial to evaluate. Following Macciò et al. (2007), we split our halo sample into unrelaxed and relaxed haloes. The latter are defined as the haloes with $\rho_{\rm rms} < 0.5$ and $x_{\rm off} < 0.07$. About 70% of the haloes in our sample qualify as relaxed haloes at $z = 0$.

To check for the effect of changing the definition of relaxed haloes, we have computed the median concentration (as shown in the next section) using different values of $x_{\rm off}$. Changing the value of this parameter by 25% (above and below 0.07) induces changes no larger than 5% in the median concentration of dark matter haloes. We conclude that choosing $x_{\rm off} = 0.07$ our results are robust enough against variations in the definition of relaxed population of haloes. In what follows we will just present results for haloes which qualify as relaxed.

3 CONCENTRATION: MASS AND REDSHIFT DEPENDENCE

In figure 1 we show the median $c_{\rm vir}-M_{\rm vir}$ relation for relaxed haloes in our sample at different redshifts. Haloes have been binned in mass bins of 0.4 dex width, the median concentration in each bin has been computed taking into account the error associated to the concentration value (see 2.1.1, and M08). In our mass range the $c_{\rm vir}-M_{\rm vir}$ relation is well fitted by a single power law at almost all redshifts. Only for $z = 2$ we see an indication that the linearity of the relation in log space seems to break, in agreement with recent findings by Klypin et al. (2010).

The best fitting power law can be written as:

$$\log(c) = a(z)\log(M_{\rm vir}/[h^{-1}\,M_\odot]) + b(z) \qquad (5)$$

The fitting parameters $a(z)$ and $b(z)$ are functions of redshift as shown in figure 2. The evolution of a and b can be itself fitted with two simple formulas that allow to reconstruct the $c_{\rm vir}-M_{\rm vir}$ relation at any redshifts:

$$a(z) = wz - m \qquad (6)$$

$$b(z) = \frac{\alpha}{(z+\gamma)} + \frac{\beta}{(z+\gamma)^2} \qquad (7)$$

Where the additional (constant) fitting parameters have been set equal to: $w = 0.029$, $m = 0.097$, $\alpha = -110.001$, $\beta = 2469.720$ and $\gamma = 16.885$. Figure 3 shows the reconstruction of the $c_{\rm vir}-M_{\rm vir}$ relation for different mass bins as a function of redshift using the approach described above. It shows that our (double) fitting formulas are able to recover
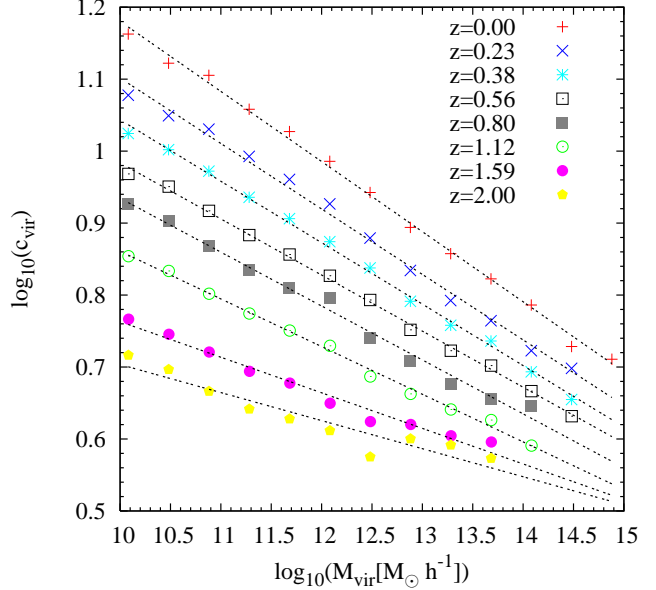

Figure 1. Mass and redshift dependence of the concentration parameter. The points show the median of the concentration as computed from the simulations, averaged for each mass bin. Lines show their respective linear fitting to eq. 5.

the original values of the halo concentration with a precision of 5%, for the whole range of masses and redshifts inspected. It has been shown by Trenti et al. (2010) that using $N_{\rm vir}$ between 100 and 400 particles is enough to get good estimates for the properties of halos, nevertheless in order to look for systematics we re-computed $c_{\rm vir}$ varying the minimum number of particle inside $R_{\rm vir}$, using 200, 500 and 1000 particles. No appreciable differences (less than 2%) were found in our results for the median. We also checked that our results do not change notably by changing the definition of "relaxed" haloes (i.e. changing the cut in $x_{\rm off}$ or $\rho_{\rm rms}$).

It is interesting to compare our results with M08, which shares some of the simulations presented in this work. Our results for the $c_{\rm vir}-M_{\rm vir}$ relation at $z = 0$ are slightly different to those presented in M08: we found $a = -0.097$ and $b = 2.155$, while M08 found $a = -0.094$ and $b = 2.099$. The difference is less than 3%, and it is mainly due to low mass haloes. In this work we included three new simulations, B30, B90 and B300$_2$. Two of these (B30 and B90) increase the statistics of our halo catalogs at the low mass end, providing a better determination of the $c_{\rm vir}-M_{\rm vir}$ relation for $M \approx 10^{11} h^{-1}\,M_\odot$. We are confident that the inclusion those new simulations led to an improvement over the results of previous works.

3.1 Understanding the concentration evolution

We want now to explore in more detail the physical mechanism driving the mass and redshift dependence of the concentration parameter, this understanding could take us to a better interpretation of the time evolution of the dark matter density profile. As $c_{\rm vir}$ is defined as the ratio between $R_{\rm vir}$ and $r_{\rm s}$ we will look at the time evolution of those quantities for different halo masses, and try to see if we can extract some physical insights about the evolution of $c_{\rm vir}$.
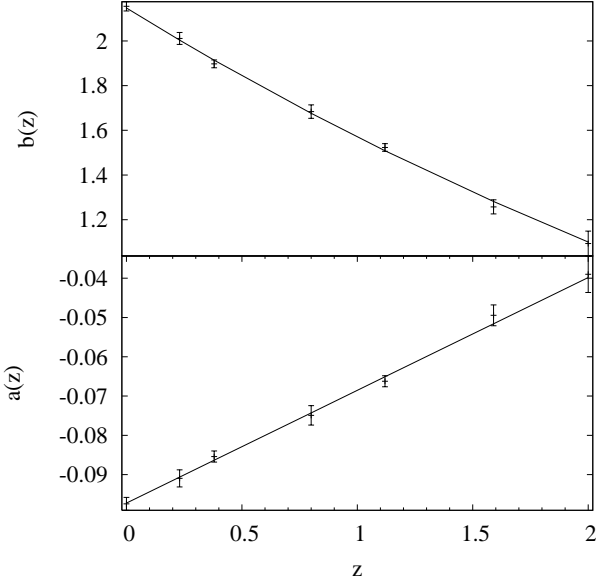
Figure 2. Redshift evolution of the parameters $a(z)$ and $b(z)$ of the linear fitting of the $c_{vir} - M_{vir}$ relation. Points represent the result of the fitting shown in figure 1 for each redshift while lines are the fit to the functions in eq:. 6 and 7. Error bars show the error obtained from the fitting to eq. 5.
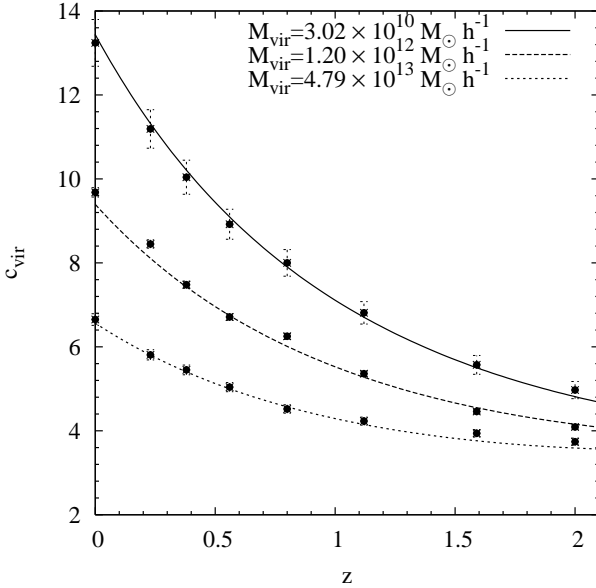

Figure 3. Reconstruction of the $c_{vir} - M_{vir}$ relation for different mass bins as a function of redshift as computed from the model fitting function, equations 5 to 7. Points show the data of our simulations while the lines show the result of the reconstruction. Error bars show the error in the median concentration for each redshift.

Since the evolution of the concentration parameter is strongly correlated to the mass growth history of the dark matter halo (e.g. Wechsler et al. 2003; Zhao et al. 2009) we need to construct merger trees for haloes in our simulation boxes. Here we briefly describe the procedure used to build

merger trees (for more details see Neistein, Macciò & Dekel 2010).

We link haloes A and B, with particle number N_A and N_B, in two consecutive snapshots at redshift z_A and z_B ($z_A < z_B$), if they success to satisfy a list of requirements:

• if $N_B < N_A$, they have at least $0.5 N_B$ particles in common

• if $N_A < N_B$, they have at least $0.5 N_A$ particles in common

• Halo B does not contribute to any other halo in z_A with more particles than it does for halo A

We will assume that the evolution of the structural properties of the halo is traced by the most massive progenitor, therefore we will present results only for the main branch of the tree. We follow along the tree the evolution of M_{vir}, R_{vir}, r_s and c_{vir}. Since individual histories of haloes can be very different we focus our study on the time evolution of the mean value of these quantities. These averages are computed binning the histories by mass at $z = 0$ with each mass bin having width of 0.4 dex. One may argue that following only the merger tree main branch of haloes indentified at z=0 could introduce a bias when comparing to the evolution of haloes at earlier cosmic times. In order to verify the stability of our results we rebuilt the merger histories for all haloes starting from z=0.5 and z=1.0 (i.e. without taking into account the future evolution of an halo, like, for example, being or not in the final catalogue at z=0). We found no differences in the evolution of the mean values for R_{vir} or M_{vir} with respect to the original merger tree built from z=0.

For the averages we include only histories with the same length, that is, histories that in the entire box evolve from the same z_{init} to $z = 0$. z_{init} was chosen by numerical-statistic reasons. As we are computing the mean on several properties of haloes in the merger histories along the time, we wanted to make sure to have at each redshift a statistically meaningful number of histories. The extension in redshift is then constrained by the resolution of our simulation and the number of histories we choose for our study. At the end we found $z_{init} \sim 3.5$ to be a good compromise. Moreover we only use histories in which the fitting of the density profile was successful in the majority of the snapshots. Any halo was allowed to be "unrelaxed" for a maximum of 2 consecutive snapshots. In this case, we used as criterion for the goodness of the density profile fit $\rho_{rms} > 0.5$. Using both our criteria of relaxation (ρ_{rms} and x_{off}) the number of histories becomes too small to be statistically meaningful. To be able to follow the histories longer in redshift we reduced the minimum number of particles per halo (inside the virial radius) from 500 (as used in the previous section) to 200. We verified that using 200 particles inside the virial radius the fitting of the density profile is still acceptable for the purposes of this section.

Finally, since we are constraining the mass histories in redshift extent, we cannot overlap data among different boxes, then we have computed average quantities for individual boxes independently. In the following we will present results coming from the B90 box, other boxes show very similar behaviours. Applying all of this selection criteria on B90 results in a set of 2300 histories with the different mass bins having between 35 and 800 halos each.
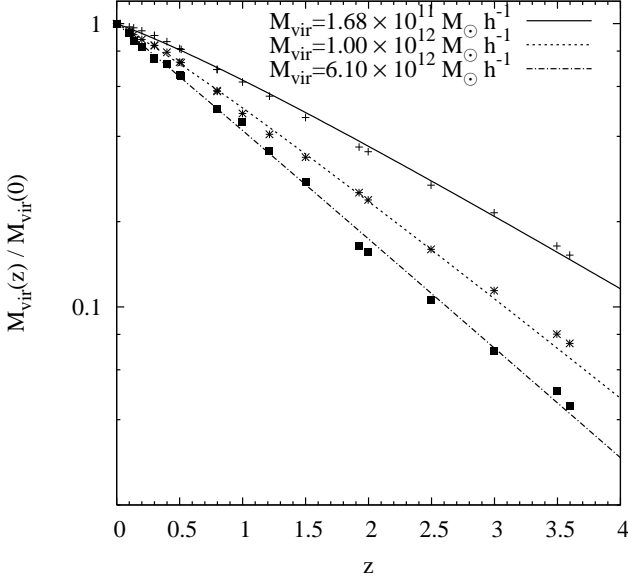
Figure 4. Mean mass accretion history for haloes in the 90 Mpc box computed for different mass bins according to their mass at z=0 (from 1.68×10^{11} to $2.8 \times 10^{13.5}$ h^{-1} $M_\odot$ with every mass bin of width 0.4 dex) as described in the main text. Here is evident the different shape of the mass growth history of haloes of different masses. Lines show the best fit to Eq 8 which shows to be a good description for all of our mass histories. The values of (γ, β) for the fit are (0.649,0.273), (0.865,0.259) and (0.900,0.045) for each line (low to high mass) respectively.

In figure 4 we show the average mass accretion history (normalized to the $z = 0$ value) for dark matter haloes in three different mass bins centered on: $1.68 \times 10^{11} h^{-1} M_\odot$, $1.0 \times 10^{12} h^{-1} M_\odot$ and $6.1 \times 10^{12} h^{-1} M_\odot$. The data are well described by the two parameter function (McBride et al. 2009)

$$M(z) = M_0(1+z)^\beta \exp(-\gamma z) \qquad (8)$$

Here M_0 is the mass at $z = 0$ and β and γ are free parameters related to the mass growth rate at low z. Note that although for most haloes $\beta \neq 0$, when $\beta = 0$ the profile assumes the exponential shape adopted by Wechsler et al. (2003) with $\gamma = \ln(2)/z_f$.

In figure 5 (top panel) we show the redshift evolution of the virial radius for haloes with final masses: $1.68 \times 10^{11} h^{-1} M_\odot$, $1.0 \times 10^{12} h^{-1} M_\odot$ and $6.1 \times 10^{12} h^{-1} M_\odot$. For all mass scales the virial radius grows with decreasing redshift reaching a maximum, and then starts a slow decrease. The redshift at which this maximum is reached depends on the mass of the halo, lower mass haloes reach that maximum earlier than more massive ones. Given the definition of $R_{\rm vir}$:

$$R_{\rm vir}(z) = \left(\frac{3M_{\rm vir}(z)}{4\pi \Delta_{\rm vir}(z)\rho_{\rm c}(z)} \right)^{1/3} \qquad (9)$$

its time evolution can be understood as follows. At high redshift the radius of the virialized region $R_{\rm vir}$ grows due to the growth of the halo mass $M(z)$ but is also subject to the effects of the cosmological background via $[\Delta_{\rm vir}(z)\rho_{\rm c}(z)]^{-1/3}$, which in this case is a slowly decreasing function with decreasing redshift. At high redshift the growth of $M(z)$ dominates, forcing $R_{\rm vir}$ to grow, at low redshift the growth rate
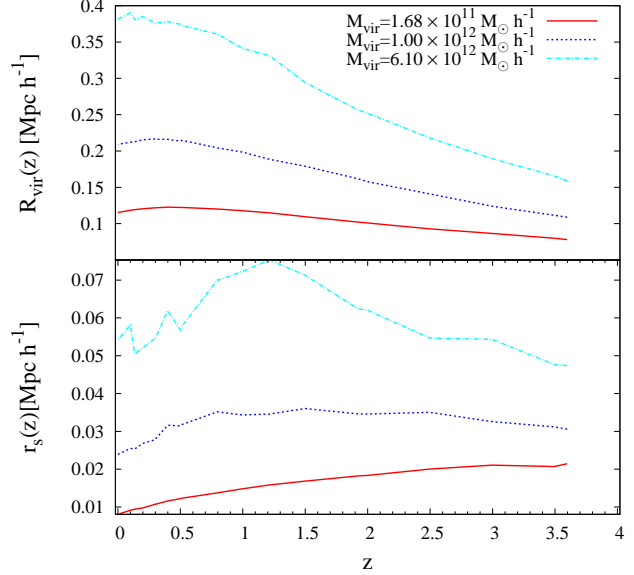

Figure 5. (Top) Time evolution of the virial radius as computed from the averaged merger histories for haloes with final mass of 1.68×10^{11}, 1.0×10^{12} and $6.1 \times 10^{12} h^{-1} M_\odot$. (Bottom) Time evolution of the averaged scale length $r_{\rm s}$ of the dark matter haloes in the same mass bins. The mass binning is the same as in figure 4.

of the halo mass becomes weaker compared to the decrease of the factor $[\Delta_{\rm vir}(z)\rho_{\rm c}(z)]^{-1/3}$, slowing the growth of $R_{\rm vir}$. This behaviour depends on the halo mass: at different redshifts haloes of different masses grow at different rates (see figure 4), on the other hand, for a given redshift, the factor $[\Delta_{\rm vir}(z)\rho_{\rm c}(z)]^{-1/3}$ is mass independent. As a result the point at which $R_{\rm vir}$ reaches its maximum happens later in time for massive haloes than for low mass ones.

The bottom panel of figure 5 shows the redshift evolution of the halo scale length $r_{\rm s}$, which has a trend similar to $R_{\rm vir}$: it grows with time, reaches a maximum and then starts to decrease. Once again the redshift at which this maximum is achieved depends on the mass of the halo, with low mass haloes reaching the maximum at earlier times.

The behaviour of $r_{\rm s}$ (and $R_{\rm vir}$) is strongly reminiscent of the behaviour of a perturbation in the spherical collapse model. It seems to suggest that the inner region of an halo (within $r_{\rm s}$) evolves in a decoupled way compared to the global perturbation (within $R_{\rm vir}$). It is then possible to model the inner region as a perturbation of density $\rho_{\rm s}$ (defined as the density inside $r_{\rm s}$) that evolves within the background density $\rho_{\rm vir}(z) = \Delta_{\rm vir}(z)\rho_{\rm c}(z)$.

In analogy with the spherical collapse model we want to look for the evolution of the density contrast of this perturbation: $\Delta_{\rm s}(z) = \rho_{\rm s}(z)/\rho_{\rm vir}(z)$. This inner density contrast is well described by the following formula:

$$\Delta_{\rm s}(z) = \frac{A}{z + \epsilon(M)} \qquad (10)$$

where $A = 50$ and $\epsilon(M) = 0.3975 \log(M_{\rm vir}(z = 0)/[h^{-1} M_\odot]) - 4.312$. Equation 10 implies that: i) $\rho_{\rm s} > \rho_{\rm vir}$ at all redshifts, ii) $\Delta_{\rm s}$ is a growing function of the redshift, implying a faster growth of the inner density with respect to the mean density of the halo and iii) $\Delta_{\rm s}$ depends on the

final mass of the halo, and it has larger values for high mass haloes.

It is now possible to interpret the evolution of the $c_{vir} - M_{vir}$ relation in the light of our findings. Figure 3 shows that the growth rate of the concentration depends on the halo mass, with low mass haloes experiencing a faster concentration evolution. Moreover, at fixed mass, the evolution of the $c_{vir} - M_{vir}$ relation is faster at lower redshifts. As can be seen from figure 5, at early times r_s grows simultaneously with R_{vir}, then, with decreasing redshift, the growth of r_s slows down, reaches a maximum, and starts to decrease. When R_{vir} grows together with r_s, the concentration of the halo stays approximately constant or slightly increases. Then when r_s slows down its growth rate and starts to "contract" the concentration of the halo grows rapidly. In the case of high mass haloes the time at which the dynamics of the inner region decouples from the outermost part, happens at later times compared to low mass haloes. As a consequence more massive haloes have a more extended period in which the concentration is a slowly growing function of time as shown in figure 3. Only in recent cosmic times, due to the late collapse of the inner part the concentration starts to grow at a higher rate also for larger masses.

A crucial point in this process is the moment when the inner part of the halo decouples from the outer one. This specific time is strongly mass dependent with smaller structures (i.e. the more non linear ones) decoupling earlier. This effect explains the change in the slope of the $c_{vir} - M_{vir}$ relation, as described in figure 2 by the evolution of $a(z)$, and also explains why a simple scaling of the redshift zero $c_{vir} - M_{vir}$ relation with a factor of the form $(1 + z)^\alpha$ (e.g. Bullock et al. 2001a) is not able to reproduce the simulated data.

4 HALO SHAPES

We now turn our attention to the evolution of halo shape with redshift and its dependence on halo mass. As was described in section 2.1.3, for each dark matter halo we compute the axis ratios $s = a_3/a_1$ and $p = a_3/a_2$, where $a_1 \geqslant a_2 \geqslant a_3$ are the major, intermediate and minor axis of the halo mass distribution. It is worth to note that in our notation using only s and p is enough to determine the shape of a dark matter halo. The condition for a halo to be oblate will be $s \sim p < 1$, while the condition to be prolate will be $s < p$ with $p \sim 1$, where the obvious condition for sphericity is $s \sim p \sim 1$ and triaxiality will be any other not filling any of the previous requirements. Figure 6 shows the evolution of the shape parameter s as a function of redshift and mass. Figure 7 is the analogue of figure 6 but for the p parameter, only results for haloes with $N_{vir} > 1000$ are shown; after several convergence tests we found that this number ensures both numerical stability of the axis determination and a fairly large statistical sample. Both figures show that on average halos are preferentially triaxial, where the most massive haloes tend to be the most ellipsoidal ones, while lower mass haloes tend to be closer to spherical, and this trend seems to be redshift independent. This seems to suggest a simple scenario where the most massive haloes are the more extended ones (and less concentrated) and hence more strongly affected by tidal torques. For each redshift
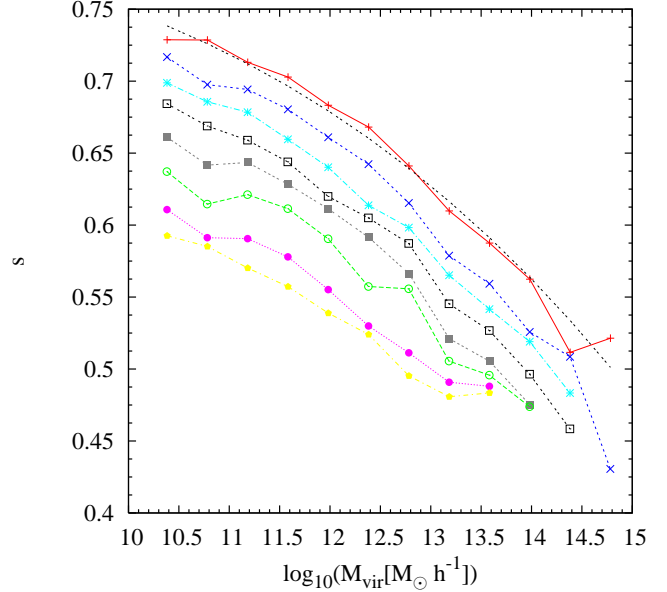
Figure 6. Mass and time evolution of the shape of dark matter haloes quantified via the $s \equiv a_3/a_1$ ratio. Points represent our data while the dashed line shows the fitting to equation 12 to $z = 0$. Similar results for the fitting are obtained for $z > 0$ and for clarity are not shown in the plot. The color code is the same used in figure 1 and shows different redshifts. Values of the fit parameters for all redshifts can be found in the appendix.

we fit the data with a power law of the form of eq: 5. The resulting parameters of this fit are listed in the Appendix.

In order to make a more direct comparison with the results of Allgood et al. (2006) we also computed the shape parameter s using only particles within the inner 30% of the virial radius $s_{0.3}$ for haloes with $N_{vir} > 4000$. The results are shown in figure 8. Allgood et al. (2006) proposed a fitting formula for the shape parameter given by,

$$s(z, M) = \alpha \left(\frac{M_{vir}}{M_*(z)} \right)^\beta \qquad (11)$$

where $M_*(z)$ is the characteristic non-linear mass at z such that the rms top-hat smoothed overdensity at scale $\sigma(M_*, z)$ is $\delta_c = 1.68$, and α and β are free parameters. The quantity $M_*(z)$ should in principle contain all the information about the cosmological model, making the other fitting parameters cosmological independent.

As already shown by M08 and Bett et al. (2007) (at $z = 0$), Eq. (11) does not provide a good fit to the data. In order to get a reasonable fit we need to add an explicit redshift dependence to the parameters α and β, while in original the model proposed by Allgood et al. , the redshift dependence of the shape parameter s was described by the quantity $M_*(z)$. A second drawback of Eq. (11) can be clearly seen in figures 6, 7 and 8. The convex-curved shape of the data deviates from a simple power-law behavior. In order to better model the data we modified Eq. (11) into

$$s(z, M) = \alpha(\log(M_{vir}/[h^{-1} \, M_\odot])^4 + \beta. \qquad (12)$$

The values of the new fitting parameters α and β are reported in table 3 in the appendix.

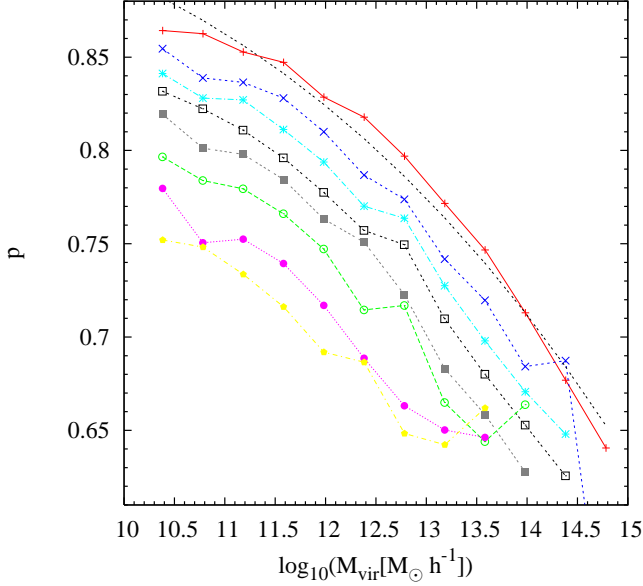Finally we compare the inner ($s_{0.3}$) to the outer shape

Figure 7. Mass and time evolution of the shape of dark matter haloes quantified via the $p \equiv a_3/a_2$ ratio. Points represent our data while the dashed line shows the fitting to equation 12 to $z = 0$. Similar results for the fitting are obtained for $z > 0$ and for clarity are not shown in the plot. The color code is the same used in figure 1 and shows different redshifts. Values of the fit parameters for all redshifts can be found in the appendix.

Figure 8. Mass and time evolution of the shape of dark matter haloes quantified via the $s_{0.3} \equiv a_3/a_1$ ratio measured at $0.3R_{\rm vir}$. Points represent our data while the dashed line shows the fitting to equation 12 to $z = 0$. Similar results for the fitting are obtained for $z > 0$ and for clarity are not shown in the plot. The color code is the same used in figure 1 and shows different redshifts. Values of the fit parameters for all redshifts can be found in the appendix.

(s); we found that haloes are slightly aspherical in their central region (5-10% effect) as already noticed by Allgood et al. (2006), who ascribed this difference to the higher number of substructure in the central region with respect to the external one. However it should be kept in mind that the internal region is the most likely to be affected by baryonic physics (e.g. Kazantzidis et al. 2004) and hence the inclusion of dissipational effects is needed in order to drive more quantitative conclusions.

5 HALO SPIN PARAMETER

The relation between spin parameter (λ') and halo mass is shown in figure 9, where for each redshift value we fit the data with a power law and in analogy with eq. 5 we denote the gradient and intercept in log space as $a(z)$ and b respectively. The parameters of these fits are shown in the Appendix. For low redshift ($z = 0; 0.23$) we found our results to be consistent with the spin parameter being almost mass independent, in agreement with Macciò et al. (2007; 2008) and Bett et al. 2007. At higher redshift ($z > 0.5$) a mass dependence of the spin starts to develop; with high mass haloes having on average a lower value of λ'. This is consistent with the results of Knebe & Power (2008), who performed a detailed study of the spin-mass relation for $z = 1$ and $z = 10$.

The evolution of the slope of the spin-mass relation is more evident in figure 10 where the values of the $a(z)$ parameter are shown (see eq: 5). As can be seen in the figure, a evolves from being consistent with 0 at $z = 0$ to negative values for increasing redshift. Knebe & Power (2008) noted that this behavior is almost insensitive to the mass binning
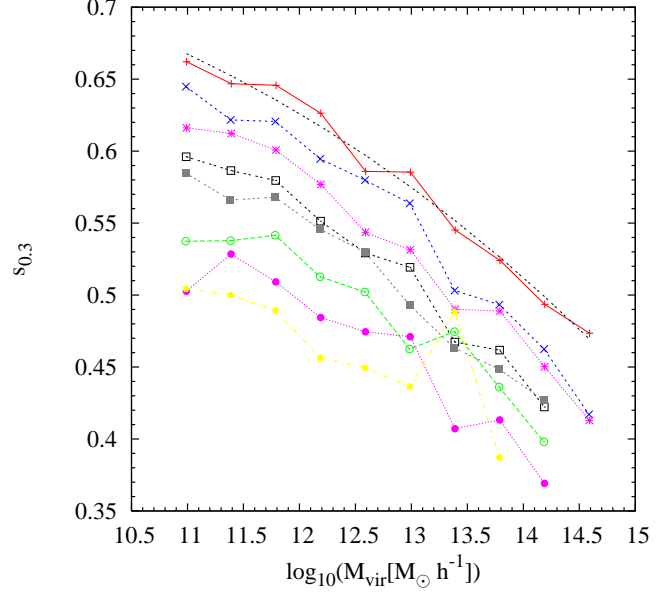
and details of the selection criteria for the relaxed halo population, but they found that the number of particles per halo is an important parameter. In order to verify the stability of our results against the minimum number of particles per halo, we show in figure 10 the redshift evolution of the slope of the spin-mass relation for two different choices of $N_{\rm vir}$, namely 500 and 1000 particles. As can be seen in the figure, the change in $N_{\rm vir}$ does change (slightly) the value of the fitted slope $a(z)$, nevertheless this change is still within the statistical errors and does not affect the overall trend.

It could be possible that the mass dependence we observe could be partially due to the mixing of different box sizes (and hence haloes with different resolution). For this purpose we analyzed the spin-mass relation independently in different boxes (B90, B180 and B300). We found no significant differences between our global analysis and the single box results. We can conclude that no numerical artifacts are affecting our results and that indeed spin parameter and halo mass are weakly correlated at high redshift.

Finally, Fig. 11 shows the distribution of spin parameters at redshifts $z = 0, 1.12$ and 2. At all redshifts the distribution is well fitted by a log-normal distribution,

$$P(\lambda') = \frac{1}{\lambda'\sqrt{2\pi}\sigma} \exp\left(-\frac{\ln^2(\lambda'/\lambda'_0)}{2\sigma^2}\right), \tag{13}$$

with $\sigma = 0.57$ and $\lambda'_0 = 0.031$. This last quantity λ'_0 shows a marginal mass dependence at high redshift as shown in figure 9.
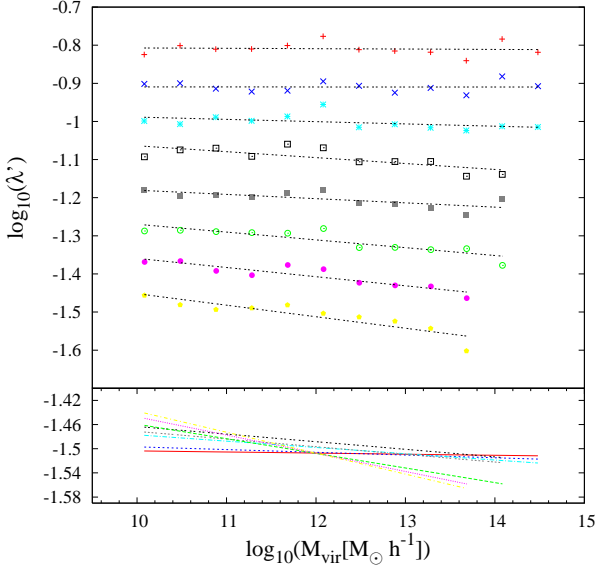
Figure 9. Mass and time evolution of the spin parameter λ'. (Top) Points are the median from our simulations while the solid lines represent the linear fitting to the data. Every line have been shifted by a constant factor of 0.1 from $z = 2$ and all of them show approximately the same mean value, nevertheless as z increases, a weak dependence of the spin on the mass of the haloes starts to become evident. The color code is the same used in figure 1 and shows different redshifts. (Bottom) Unshifted linear fitting to λ'. The color code of each line is the same used in the plot on top.
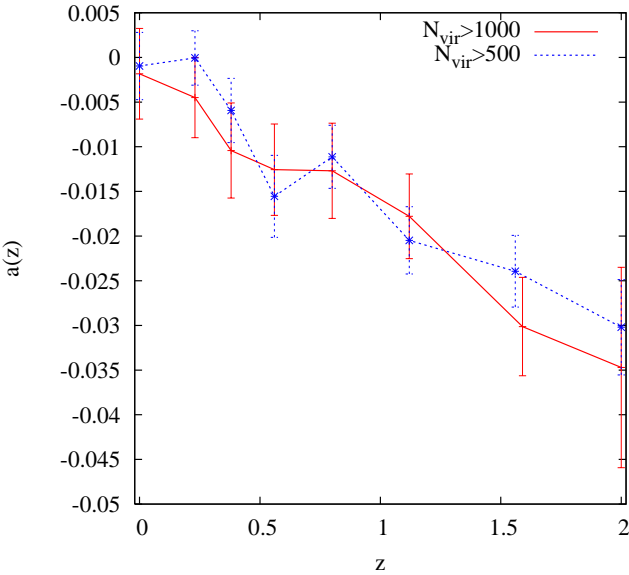

Figure 10. Time evolution of the parameters of fitting $a(z)$ and $b(z)$ to equation 5 for the spin-mass relation for haloes with at least 500 (blue) and 1000 (red) particles inside the virial radius. Error bars show the error in the value of the parameter a given from the fitting.
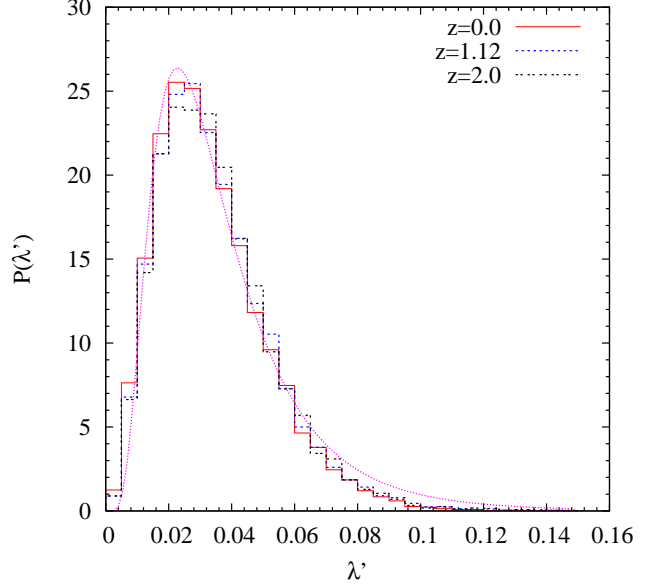

Figure 11. Distribution of halo spin parameter λ' at redshifts $z = 0, 1, 2$, compared to a log-normal distribution with $\lambda'_0 = 0.031$ and $\sigma = 0.57$.

6 DISCUSSION AND CONCLUSIONS

In this work we present a detailed analysis of a large set of N-body simulations performed within a WMAP 5th year ΛCDM cosmology (Komatsu et al. 2009). We study the relation between structural properties of dark matter haloes (concentration, spin and shape) with mass, and the evolution of such scaling relations with redshift. We span the entire mass range important for galaxy formation $[10^{10} : 10^{15} h^{-1} \, M_\odot]$ and a redshift range from $z = 0$ to $z = 2$.

We present results for "relaxed" haloes, defined according to the criteria suggested by Macciò et al. (2007). In our mass and redshift range the $c_{vir} - M_{vir}$ relation always follows a power law behavior. We confirmed that the redshift dependence of such relation is more complex than a simple $(1 + z)^{-1}$ scaling as proposed by Bullock et al. 2001a, with both the normalization and the slope of the relation changing with cosmic time. We also found that for increasing redshifts ($z \approx 2$) the power law behaviour seems to break in agreement with recent studies (e.g. Klypin et al. 2010). Thanks to our multiple box simulations we tested our results against resolution effects and find them to be stable once a sufficient large number of particles is used $N_{vir} > 500$.

Recently two other works have addressed the topic of the evolution of the $c_{vir} - M_{vir}$ relation, Zhao et al. (2009) and Klypin et al. (2010). When compared with the model proposed in Zhao et al. (2009) our results show a very good agreement at the low mass end (possibly due to the fact that both halo samples have more or less the same level of resolution). For high masses we find a slightly higher difference but never exceeding few percent. The comparison with Klypin et al. is less straightforward since they used a different method to compute concentrations, based on the circular velocity of the halo instead of directly fitting the density profile. Moreover they use all haloes in their simulation volume without any distinction between relaxed and unrelaxed. Our results are in qualitative agreement with the model proposed by

Klypin et al. for the evolution of the $c_{\mathrm{vir}} - M_{\mathrm{vir}}$ relation but there are differences of the order of 8%. It is then interesting to ask ourselves if these differences arise from the different method used to compute c_{vir}.

For this purpose we applied to our B90 box (which has roughly the same resolution as the Bolshoi simulation of Klypin et al. 2010) the method proposed by Klypin to compute the concentration, based on the relation between mass and maximum circular velocity. To be consistent with Klypin et al. 2010 we considered all haloes in our sample, without making any distinction between relaxed and unrelaxed. We find that the different methods to compute c_{vir} do not introduce any systematic bias, being perfectly consistent. Nevertheless we found that at fixed mass our haloes have a lower circular velocity compared to the Klypin et al. (2010) results. Taking into account the explicit dependence of the concentration on V_{c} we are keen to conclude that part of the difference in $c_{\mathrm{vir}} - M_{\mathrm{vir}}$ relation could be due the slightly different values of the cosmological parameters and primordial power spectral index.

Another interesting result regards the effect of including unrelaxed haloes. Klypin et al. (2010) did not make any attempts of removing unrelaxed haloes; this is in principle justified because their concentrations are obtained from an integral quantity (V_{c}) which is less affected by the dynamical status of the halo with respect to a differential one like ρ. On the other hand by applying Klypin's method to our B90 box we found that the $V_{\mathrm{c}} - M$ relation has a systematic shift ($\approx 6\%$) towards higher values when it is computed for "relaxed" haloes instead than for all haloes. This results in a systematic bias, towards lower concentrations, for the "all" sample with respect to the relaxed one.

Finally Zhao et al. (2009) and Klypin et al. (2010) found that the concentration may have a minimum value close to 3.5-4.5 at redshift close to 4. Unfortunately our simulations do not have enough resolution to get a statistical valid halo sample at such a high redshift, so we cannot confirm such a finding, even if we do see some evidence of a breaking of a simple power law behaviour for the $c_{\mathrm{vir}} - M_{\mathrm{vir}}$ relation at $z = 2$. Let us stress one more time that the fitting formula we proposed in this work are valid only in the test redshift range [0-2] and should not be extrapolated at higher redshifts.

In order to improve our understanding on the redshift evolution of the $c_{\mathrm{vir}} - M_{\mathrm{vir}}$ relation we look at the individual evolution with time of r_{s} and R_{vir}. Both these length scales grow with decreasing redshift until a maximum is reached, then they start to decrease towards $z = 0$. There is a clear analogy between the collapse of a linear perturbation and the behaviour of r_{s} and R_{vir}. We found that we can model the evolution of the inner part of the halo (within r_{s}) as a decoupled spherical perturbation growing inside the central region of the halo. The temporal offset between the "turning points" of the perturbations associated with r_{s} and R_{vir} is able to explain the observed redshift evolution of the $c_{\mathrm{vir}} - M_{\mathrm{vir}}$ relation; which strongly deviates from a simple $(1 + z)^{\alpha}$ scaling of the $z = 0$ relation. As a final remark we would like to stress that our results refer to the dark matter distrubution in the absence of a collisional component. Although it has been shown that the inclusion of baryonic physics may affect the properties of the dark matter, it also known that the strength of this effect strongly depends on the implemented baryonic physics (Duffy et al. 2010, Gover-

nato et al. 2010). The dark matter distribution in real haloes is still under debate and a comparison of pure dark matter results with observations should be preformed with extreme caution.

We then investigate the mass and redshift dependence of the axis ratio (p and s) of dark matter haloes. Our results are in agreement with previous studies and show that although on average haloes in our simulations are preferentially triaxial at all masses and redshifts, low mass haloes are more spherical than high mass ones and, at any mass, central regions are more aspherical than outer ones. We find a more complex evolution of the shape-mass relation with redshift with respect to the model proposed by Allgood et al. (2006). We propose a new fitting function (that deviates from a simple power law) that is able to reproduce our data in the whole redshift and mass range.

Finally we studied the evolution of the spin parameter λ'. At redshift zero we confirm the results of Macció et al. (2007; 2008), who found the spin parameter to be mass independent. For increasing redshift there is evidence of a correlation between halo mass and spin: on average, more massive haloes have lower values of the spin parameter. This is in agreement with recent findings at very high redshift ($z = 10$) by Knebe & Power (2008). As already speculated by those authors, since disk sizes are to first order proportional to the spin parameter (Mo et al. 1998), a lower spin parameter for high mass haloes could make their central stellar and gaseous body more compact and hence allowing more efficient star formation. In addition this could affect the evolution of the size-mass relation of galaxy disks, which is usually modeled by assuming λ is independent of mass and redshift (Mao, Mo & White 1998; Somerville et al. 2008; Firmani & Avila-Reese 2009; Dutton et al. 2010).

However, in our simulations the differences in median spin parameters at $z = 2$ compared to $z = 0$ are at most 15%, and thus the consequences to observables such as the size-mass relation of disk galaxies are likely to be small. Furthermore, baryonic effects such as supernova driven outflows and inefficient cooling can modify spin parameters by much larger amounts (factors of ~ 2) (Dutton & van den Bosch 2009). Thus it is unlikely that the mass dependence on halo spin that we observe in our simulations at $z = 2$ will have an unambiguous observational signature.

REFERENCES

Allgood, B., Flores, R. A., Primack, J. R., Kravtsov, A. V., Wechsler, R. H., Faltenbacher, A., & Bullock, J. S. 2006, MNRAS, 367, 1781

Antonuccio-Delogu, V., Dobrotka, A., Becciani, U., Cielo, S., Giocoli, C., Maccio', A, & Romeo, A. 2010, arXiv:1003.3877

Bailin, J., & Steinmetz, M. 2005, ApJ, 627, 647

Bertschinger, E. 2001, ApJS, 137, 1

Bett, P., Eke, V., Frenk, C. S., Jenkins, A., Helly, J., & Navarro, J. 2007, MNRAS, 376, 215

Bett, P., Eke, V., Frenk, C. S., Jenkins, A., & Okamoto, T. 2010, MNRAS, 404, 1137

Bryan, G. L., & Norman, M. L. 1998, ApJ, 495, 80

Bullock, J. S., Kolatt, T. S., Sigad, Y., Somerville, R. S., Kravtsov, A. V., Klypin, A. A., Primack, J. R., & Dekel, A. 2001a, MNRAS, 321, 559

Bullock, J. S., Dekel, A., Kolatt, T. S., Kravtsov, A. V., Klypin, A. A., Porciani, C., & Primack, J. R. 2001b, ApJ, 555, 240

Comerford, J. M., & Natarajan, P. 2007, MNRAS, 379, 190

Davis, A. J., & Natarajan, P. 2009, MNRAS, 393, 1498

Duffy, A. R., Schaye, J., Kay, S. T., & Dalla Vecchia, C. 2008, MNRAS, 390, L64

Duffy, A. R., Schaye, J., Kay, S. T., Vecchia, C. D., Battye, R. A., & Booth, C. M. 2010, MNRAS, 624

Dutton, A. A., van den Bosch, F. C., Dekel, A., & Courteau, S. 2007, ApJ, 654, 27

Dutton, A. A., & van den Bosch, F. C. 2009, MNRAS, 396, 141

Dutton, A. A., et al. 2010, arXiv:1006.3558, MNRAS in press

Eke, V. R., Navarro, J. F., & Steinmetz, M. 2001, ApJ, 554, 114

Firmani, C., & Avila-Reese, V. 2009, MNRAS, 396, 1675

Gao, L., Navarro, J. F., Cole, S., Frenk, C. S., White, S. D. M., Springel, V., Jenkins, A., & Neto, A. F. 2008, MNRAS, 387, 536

Gnedin, O. Y., Kravtsov, A. V., Klypin, A. A., & Nagai, D. 2004, ApJ, 616, 16

Gottlöber, S., & Yepes, G. 2007, ApJ, 664, 117

Hahn, O., Carollo, C. M., Porciani, C., & Dekel, A. 2007, MNRAS, 381, 41

Hahn, O., Porciani, C., Carollo, C. M., & Dekel, A. 2007, MNRAS, 375, 489

Komatsu E., et al., 2009, ApJS, 180, 330

Kuhlen, M., Strigari, L. E., Zentner, A. R., Bullock, J. S., & Primack, J. R. 2005, MNRAS, 357, 387

Jing, Y. P., & Suto, Y. 2002, ApJ, 574, 538

Jing, Y. P. 2000, ApJ, 535, 30

Kazantzidis, S., Kravtsov, A. V., Zentner, A. R., Allgood, B., Nagai, D., & Moore, B. 2004, ApJ, 611, L73

Klypin, A., Trujillo-Gomez, S., & Primack, J. 2010, arXiv:1002.3660

Knebe, A., & Power, C. 2008, ApJ, 678, 621

Knebe, A., Libeskind, N. I., Knollmann, S. R., Yepes, G., Gottlöber, S., & Hoffman, Y. 2010, MNRAS, 405, 1119

Libeskind, N. I., Yepes, G., Knebe, A., Gottlöber, S., Hoffman, Y., & Knollmann, S. R. 2010, MNRAS, 401, 1889

Macciò, A. V., Murante, G., & Bonometto, S. P. 2003, ApJ, 588, 35

Macciò, A. V., Dutton, A. A., van den Bosch, F. C., Moore, B., Potter, D., & Stadel, J. 2007, MNRAS, 378, 55

Macciò, A. V., Dutton, A. A., & van den Bosch, F. C. 2008, MNRAS, 391, 1940 (M08)

Mao, S., Mo, H. J., & White, S. D. M. 1998, MNRAS, 297, L71

McBride, J., Fakhouri, O., & Ma, C.-P. 2009, MNRAS, 398, 1858

Mo, H. J., Mao, S., & White, S. D. M. 1998, MNRAS, 295, 319

Navarro, J. F., Frenk, C. S., & White, S. D. M. 1997, ApJ, 490, 493

Neistein, E., Macciò, A. V., & Dekel, A. 2010, MNRAS, 403, 984

Neto, A. F., et al. 2007, MNRAS, 381, 1450

Somerville, R. S., et al. 2008, ApJ, 672, 776

Spergel, D. N., et al. 2007, ApJS, 170, 377

Stadel, J. G. 2001, Ph.D. Thesis.

Trenti, M., Smith, B. D., Hallman, E. J., Skillman, S. W., & Shull, J. M. 2010, ApJ, 711, 1198

Wechsler, R. H., Bullock, J. S., Primack, J. R., Kravtsov, A. V., & Dekel, A. 2002, ApJ, 568, 52

White, S. D. M., & Rees, M. J. 1978, MNRAS, 183, 341

Zhao, D. H., Mo, H. J., Jing, Y. P., Börner, G. 2003, MNRAS, 339, 12

Zhao, D. H., Jing, Y. P., Mo, H. J., Börner, G. 2003, ApJ, 597, L9

Zhao, D. H., Jing, Y. P., Mo, H. J., Börner, G. 2009, ApJ, 707, 354

APPENDIX A: DETAILED VALUES FOR THE PARAMETERS OF THE DIFFERENT FITS PRESENTED IN THE MAIN BODY OF THE PAPER.

We give in this appendix a complete set of tables with the value of all the fitting parameters presented in the paper. All fits to the data are performed for the functional form $\log(\psi) = a \log(M_{\mathrm{vir}}) + b$ where ψ can be either c_{vir}, λ', s or p and where M_{vir} is in units of $10^{10} h^{-1} \mathrm{M}_\odot$. We stress on the validity of our results in the range of redshifts between 0 and 2. Nevertheless individual fits are valid in the individual mass ranges $[10^{10} h^{-1} \mathrm{M}_\odot, 10^{15} h^{-1} \mathrm{M}_\odot]$ for z=0, $[10^{10} h^{-1} \mathrm{M}_\odot, \sim 3.16^{14} h^{-1} \mathrm{M}_\odot]$ for z=0.23, 0.38 and 0.56, $[10^{10} h^{-1} \mathrm{M}_\odot, \sim 1.26^{14} h^{-1} \mathrm{M}_\odot]$ for z=0.8, and 1.12 and $[10^{10} h^{-1} \mathrm{M}_\odot, \sim 5.0^{13} h^{-1} \mathrm{M}_\odot]$ for z=1.59, and 2.0.

We present in table 2, just for completeness, the fitting of the shape paramaters to $\log(\psi) = a \log(M_{\mathrm{vir}}) + b$ for all masses and redshifts. In table 3 we present the fit to Eq. 12 to the shape parameters s, p and $s_{0.3}$.

This paper has been typeset from a TEX/ LATEX file prepared by the author.

Table 2. Values of the fit parameters for the data presented in the paper. $\log(c_{\rm vir})$, $\log(\lambda')$ as computed from haloes with at least 500 and 1000 particles inside the virial radius and $\log(s)$ and $\log(p)$ as computed for haloes with more than 4000 particles inside the virial radius. All fits where done to the function $\log(\psi) = a\log(M_{\rm vir}) + b$. N haloes is the total number of relaxed haloes used at that redshift to compute the mean and median values.

Redshift	N haloes	a	Δa	b	Δb
		$\log(c_{\rm vir})$ (Nmin = 500)			
0	23777	-0.097	0.002	2.155	0.021
0.23	22358	-0.091	0.002	2.011	0.027
0.38	20906	-0.085	0.001	1.897	0.018
0.56	19475	-0.078	0.001	1.763	0.013
0.8	17696	-0.075	0.002	1.684	0.030
1.12	14960	-0.066	0.001	1.523	0.017
1.59	11888	-0.049	0.003	1.257	0.032
2.0	9290	-0.039	0.005	1.093	0.055
		$\log(\lambda')$ (Nmin = 500)			
0	23777	-0.001	0.004	-1.497	0.046
0.23	22358	-0.000	0.003	-1.509	0.038
0.38	20906	-0.006	0.004	-1.429	0.044
0.56	19475	-0.015	0.005	-1.308	0.056
0.8	17696	-0.011	0.003	-1.369	0.043
1.12	14960	-0.020	0.004	-1.265	0.046
1.59	11888	-0.024	0.004	-1.220	0.048
2.0	9290	-0.030	0.005	-1.150	0.064
		$\log(\lambda')$ (Nmin = 1000)			
0	12427	-0.002	0.005	-1.485	0.063
0.23	11563	-0.004	0.004	-1.452	0.056
0.38	10753	-0.010	0.005	-1.373	0.066
0.56	10049	-0.012	0.005	-1.337	0.062
0.8	8942	-0.013	0.005	-1.344	0.065
1.12	7482	-0.016	0.005	-1.292	0.058
1.59	5851	-0.030	0.005	-1.146	0.067
2.0	4404	-0.035	0.011	-1.091	0.137
		$\log(s)$ (Nmin = 4000)			
0	3102	-0.039	0.006	0.386	0.079
0.23	2785	-0.033	0.003	0.294	0.044
0.38	2523	-0.036	0.004	0.322	0.059
0.56	2281	-0.035	0.003	0.303	0.034
0.8	1972	-0.038	0.004	0.333	0.055
1.12	1588	-0.033	0.005	0.260	0.063
1.59	1211	-0.025	0.005	0.153	0.059
2.0	879	-0.024	0.010	0.133	0.123
		$\log(p)$ (Nmin = 4000)			
0	3102	-0.051	0.007	0.443	0.096
0.23	2785	-0.044	0.005	0.344	0.062
0.38	2523	-0.043	0.005	0.318	0.065
0.56	2281	-0.044	0.004	0.314	0.051
0.8	1972	-0.044	0.006	0.298	0.071
1.12	1588	-0.039	0.006	0.224	0.076
1.59	1211	-0.034	0.005	0.145	0.059
2.0	879	-0.032	0.012	0.112	0.147

Table 3. Values of the fit parameters for the data presented in the paper s, p and $s_{0.3}$ as computed for haloes with more than 1000 and 4000 particles inside the virial radius respectively. All fits where done to the function $\psi = \alpha[\log(M_{\rm vir})]^4 + \beta$. N haloes is the total number of relaxed haloes used at that redshift to compute the mean and median values.

Redshift	N haloes	$\alpha(\times 10^{-6})$	$\Delta\alpha(\times 10^{-7})$	β	$\Delta\beta$
		s (Nmin = 1000)			
0.0	12426	-6.566	2.760	0.815	0.008
0.23	11563	-7.622	2.818	0.815	0.008
0.38	10753	-7.009	1.185	0.783	0.003
0.56	10049	-7.215	1.484	0.771	0.004
0.8	8942	-7.173	3.320	0.751	0.008
1.12	7482	-6.388	3.945	0.714	0.010
1.59	5851	-5.932	3.760	0.677	0.008
2.0	4404	-5.512	3.936	0.655	0.009
		p (Nmin = 1000)			
0.0	12426	-6.345	2.510	0.955	0.007
0.23	11563	-7.396	7.872	0.955	0.023
0.38	10753	-6.452	2.024	0.923	0.005
0.56	10049	-6.802	1.755	0.916	0.005
0.8	8942	-7.539	2.984	0.916	0.007
1.12	7482	-5.992	5.600	0.867	0.014
1.59	5851	-6.299	4.812	0.845	0.011
2.0	4404	-5.118	7.149	0.808	0.016
		$s_{0.3}$ (Nmin = 4000)			
0	3102	-6.464	2.709	0.760	0.008
0.23	2785	-7.484	3.404	0.760	0.010
0.38	2523	-6.776	2.803	0.722	0.008
0.56	2281	-6.870	3.522	0.703	0.010
0.8	1972	-6.444	3.397	0.682	0.009
1.12	1588	-5.487	5.210	0.632	0.014
1.59	1211	-6.441	7.297	0.632	0.020
2.0	879	-4.050	0.138	0.562	0.035